Effect of transition metal substitution on the flexibility and thermal properties of MOF-based solid-solid phase change materials

Kieran Griffiths,[1] Nathan R. Halcovitch[1] and John M. Griffin[1,2]*

1. Department of Chemistry, Lancaster University, Lancaster, LA1 4YB, UK
2. Materials Science Institute, Lancaster University, Lancaster, LA1 4YB, UK

*Corresponding author. Email j.griffin@lancaster.ac.uk

ABSTRACT: A series of azobenzene-loaded metal-organic frameworks was synthesised with the general formula $M_2(BDC)_2(DABCO)(AB)_x$ (M = Zn, Co, Ni, Cu; BDC = 1,4-benzenedicarboxylate, DABCO = 1,4-diazabicyclo[2.2.2]octane; AB = azobenzene), herein named **M-1**⊃AB_x. Upon occlusion of AB, each framework undergoes guest-induced breathing whereby the pores contract around the AB molecules forming a narrow-pore (*np*) framework. The loading level of the framework is found to be very sensitive to the synthetic protocol and although the stable loading level is close to **M-1**⊃$AB_{1.0}$, higher loading levels can be achieved for the Zn, Co and Ni frameworks prior to vacuum treatment, with a maximum composition for the Zn framework of **Zn-1**⊃$AB_{1.3}$. The degree of pore contraction upon loading is modulated by the inherent flexibility of the metal-carboxylate paddlewheel unit in the framework, with the **Zn-**

1⊃$AB_{1.0}$ showing the biggest contraction of 6.2% and the more rigid **Cu-1**⊃$AB_{1.0}$ contracting by only 1.7%. Upon heating, each composite shows a temperature-induced phase transition to an open-pore (*op*) framework, and the enthalpy and onset temperatures of the phase transition is affected by the framework flexibility. For all composites, UV irradiation causes *trans* → *cis* isomerisation of the occluded AB molecules. The population of *cis*-AB at the photostationary state and the thermal stability of the occluded *cis*-AB molecules is also found to correlate with the flexibility of the framework. Over a full heating-cooling cycle between 0 – 200 °C, the energy stored within the metastable *cis*-AB molecules is released as heat, with a maximum energy density of 28.9 J g^{-1} for **Zn-1**⊃$AB_{1.0}$. These findings suggest that controlled confinement of photoswitches within flexible frameworks is a potential strategy for the development of solid-solid phase change materials for energy storage.

1. INTRODUCTION

Energy storage technologies are gaining increased attention to bridge the gap between energy supply and demand, and this is particularly important for intermittent renewable energy sources such as solar and wind. Phase change materials (PCMs) are widely studied and used for the storage of thermal energy.[1–8] PCMs store latent heat above a phase transition temperature and the energy is released through reversal of the phase change upon cooling. Many PCMs are based on solid-liquid phase transitions, although there is increasing interest in solid-solid (ss)-PCMs in which energy is stored via a structural rearrangement or crystallographic phase transition while the material remains in the solid state.[1,5,7] A key consideration for both conventional PCMs and ss-PCMs is that they must be maintained above the phase-transition temperature for the duration of energy storage, thus requiring the use of both thermal insulation and additional energy input. However, some phase changes can be triggered by other methods, for example some ceramic ss-

PCMs have been shown to undergo their phase change when placed under high pressure.[9] Solid-liquid PCMs have also been demonstrated in commercial hand-warmers (saturated salt solutions) to trigger using metal clips, and azobenzene dopants have also been added to *n*-fatty acids[10] as well as fatty alcohols and *n*-alkanes[11] to enable light-induced triggering of the phase transformation. Additionally, it has been demonstrated for some PCM systems such as polyethylene glycol that the phase-change temperature can be tuned for a particular application, for example by altering the molecular weight.[12] These findings serve to broaden the functional temperature range of PCMs.

An alternative to PCMs are solar thermal fuels (STFs) that store solar energy through light-induced changes in chemical or isomeric structure.[13–17] In contrast to PCMs, the energy can be stored at ambient temperature before being released on demand as heat by using either heat or light to trigger reconversion to the ground-state structure. A number of STF systems have been demonstrated in the liquid[18–20] and solid-state.[21–25] Recent development continues to increase the energy density of STF materials, as well as to lengthen the energy storage lifetime.[13,14,19,26] Recently, we demonstrated that a composite material formed by the occlusion of azobenzene (AB) within the pores of a metal-organic framework (MOF) functions as a hybrid ss-PCM and STF material.[27] The MOF is based upon the flexible framework $Zn(BDC)_2(DABCO)$ (BDC = 1,4-benzenedicarboxylate, DABCO = 1,4-diazabicyclo[2.2.2]octane).[28–31] Exposure to UV light causes the occluded *trans*-AB molecules to isomerise to metastable *cis*-AB.[32] The energy stored within the *cis*-AB-MOF composite is released over a complete heating and cooling cycle between ambient temperature and 200 °C. The mechanism of energy release involves a reversible, thermally-driven structural phase change coupled with exothermic heat release as the occluded *cis*-AB molecules revert to the ground-state *trans* isomer. Previous work on structurally similar "breathable" MOF

systems has shown that the nature of the metal ion can modulate the flexibility of the framework, which in turn has a large effect on the phase transition temperature and enthalpies.[33–36] So far, the $M(BDC)_2(DABCO)(AB)$ system has only been studied for the case of M = Zn and some details of the energy storage and release mechanism remain poorly understood. A better understanding of the influence of the metal centre on the thermal properties of this system will provide greater insight into the energy storage and release mechanism, and potentially allow for parameters such as the phase transition temperature and enthalpy to be tuned for particular applications.

Herein, we present a systematic study of the effect of substitution of the metal centre on the structural and thermal properties of the $M(BDC)_2(DABCO)(AB)$ system, abbreviated as **M-1**⊃AB_x where M = Zn, Co, Ni or Cu. This work builds on the previous literature for related breathable systems by providing insight into how the intrinsic framework flexibility affects the structure and thermal properites, as well as the photoswitching behaviour of the AB guest molecules. We find, for all frameworks, the amount of AB occluded within the pores is highly sensitive to the duration of vacuum treatment that is typically used in the loading procedure. When this is considered, the nature of the metal centre is found to have a marked influence on the breathing behaviour of the framework and the photostationary state of the AB guest. This alters the thermal properties and therefore the energy densities of the composites, as well as the duration for which energy can be stored.

2. EXPERIMENTAL SECTION

Synthesis of M-1. All reagents were obtained from Fluorochem and used without further purification. $M_2(BDC)_2(DABCO)$ (**M-1**, M = Ni, Co, Zn, Cu) was synthesised according to previously reported synthetic procedures.[33,37–39] $M(NO_3)_2 \bullet 6H_2O$ (M = Ni, Co, Zn, 1.68 mmol) or $Cu(NO_3)_2.3H_2O$ (1.68 mmol) was sonicated in *N*,*N*-dimethylformamide (DMF, 20 mL) until fully dissolved, 1,4-dibenzendicarboxylic acid (0.28 g, 1.68 mmol) and DABCO (0.093 g, 0.84 mmol) were then added. The reactant solution was placed in a stainless-steel autoclave (Parr) with a Teflon lining with a 50 mL capacity. The solution was heated at 120 ˚C for 48 h and left to cool to room temperature. The colourless (**Zn-1**, yield - 81%),[27] green (**Ni-1**, yield – 77%), dark blue (Co-1, yield - 79%) and teal (**Cu-1**, yield – 70%) crystals were collected via vacuum filtration and washed with DMF (3 x 30 mL) before drying under ambient conditions. Phase purity of the compounds was confirmed by LeBail fitting of the XRPD patterns, shown in Figure S2.

Loading of M-1 with AB. Samples of **M-1** were loaded with AB using a previously published melt-infiltration procedure.[27,32] As-prepared samples of **M-1** were first heated at 120 °C under vacuum for 24 h to remove DMF solvent molecules. 300 mg of the evacuated material was then mixed with a defined mass of *trans*-AB and heated at 120 °C for 3 h. Excess AB was removed by heating at 120 °C under vacuum for between 1 - 6 h.

Quantification of AB loading level by UV-vis spectroscopy. UV-vis data was collected on a Cary 60 UV/VIS spectrophotometer with a quartz cell (3 mL) within a 200-600 nm range. A calibration curve with known concentrations of *trans*-AB was constructed (Figure S16). AB was extracted from **M-1**$\supset AB_x$ (50 mg) using MeOH (10 mL x 4) and the filtrate was collected. The

orange filtrate was combined, and the solution was diluted to a volume of 50 mL. The calculations for the loading levels (**M-1**: AB) of **M-1**⊃$AB_{1.0}$ are shown in Figure S15, where **Ni-1**⊃$AB_{1.0}$ (1.0: 0.99), **Co-1**⊃$AB_{1.0}$ (1.0: 0.99), and **Cu-1**⊃$AB_{1.0}$ (1.0: 0.94). These values are consistent with the mass differences observed in TGA analysis (S26).

Photostationary state determination of irradiated M-1⊃$AB_{1.0}$ composites. 25 mg of **M-1**⊃$AB_{1.0}$ was suspended in MeOH-d_4 (0.5 mL) in an Eppendorf and shaken. The Eppendorf was centrifuged to separate the solid from the solution. A Bruker Avance III 400 NMR spectrometer with a 5 mm ^{1}H-X broadband observe probe was used to collect ^{1}H NMR data. The population ratio of *trans*-AB and *cis*-AB isomers was determined from integration of *trans* and *cis* resonances in the ^{1}H NMR spectrum based on literature values. The remaining solid was digested in DCl (1.5 mL) and DMSO-d_6 (1.5 mL) and placed in a stainless-steel autoclave (Parr) with a Teflon lining with a 50 mL capacity. The suspension was heated for 12 h at 100 °C to yield a transparent solution. The ^{1}H NMR spectrum of the solution was taken, and no residual *trans*-AB or *cis*-AB resonances were detected. The process was repeated three separate times and *cis*/*trans* ratios were consistent.

UV light irradiation procedure. Samples were irradiated with an OmniCure LX5 LED Head with a power of 425 mW and a 3 mm focusing lens. 50 mg of finely ground **M-1**⊃AB_x was spread homogenously over a microscope slide. The powder was spread into a circle with a 1 cm radius which was approximately 0.5 mm thick so that irradiation was approximately uniform. The slide was placed under 365 nm light at a distance of 5 cm. The beam was set to 50% intensity and exposed for a fixed duration. The sample was incrementally agitated to allow all particulates to be exposed to the beam.

XRPD. X-ray powder diffraction (XRPD) patterns were measured with a Rigaku SmartLab X-ray diffractometer with a 9 kW rotating anode Cu-source equipped with a high-resolution Vertical θ/θ 4-Circle Goniometer and D/teX-ULTRA 250 High-Speed Position-Sensitive Detector System in reflectance mode. The system was configured with parallel-beam optics and a Ge(220) 2 bounce monochromator on the incident side. Powdered solid samples were prepared on glass slides. The measurements were performed as θ/2θ scans with a step size of 0.01 degrees. Variable-temperature measurements were carried out by loading the powder sample into 1 mm diameter thin-walled (0.1mm) borosilicate capillaries, with the capillary loosely sealed with silicone grease to allow for pressure to be released upon heating. The capillary was loaded on a BTS-500 Anton Parr heating stage equipped with a zero-background holder and mounted on a Rigaku SmartLab (9 kW) diffractometer. The heating stage was purged with nitrogen for 30 minutes prior to analysis. The diffractometer was used with parallel-beams optics and a 5 degree soller slit, and a Dtex-250 Ultra 1D detector. The sample run was carried out using a 2-theta scan with a step size of 0.01 degrees 2-theta, and a scanning rate of 4 degrees per minute.

3. RESULTS AND DISCUSSION

2.1 Framework contraction in $M(BDC)_2(DABCO)$ MOFs upon AB occlusion

The $M(BDC)_2(DABCO)$ structure is formed from paddlewheel units composed of divalent metal cations which are bridged by BDC linkers to form 2D layers. These layers are bridged by DABCO to form a 3D framework (Figure 1). Yanai *et al*. have previously shown that the occlusion of *trans*-AB within the pores of **Zn-1** leads to guest-induced breathing of the framework signified by a transition from the tetragonal (*P*4/*mmm*) open structure to an orthorhombic (*Cmmm*) structure with

reduced pore volume.[32] Recently, we re-examined the structural changes in **Zn-1** upon incorporation of *trans*-AB and found that, at a loading level of 0.5 AB molecules per **Zn-1** formula unit (**Zn-1**⊃$AB_{0.5}$), the orthorhombic structure starts to transform to another tetragonal structure (*I*4/*mcm*) characterised by bent BDC linkers which are aligned along the $a = b$ axes. While the length of the c axis remains almost unchanged, the bent linkers reduce the lengths of the $a = b$ axes by 3.2% compared to the guest-free structure, resulting in a contraction of the reduced unit cell volume by 6.5%. At a loading level of one AB molecules per **Zn-1** formula unit (**Zn-1**⊃$AB_{1.0}$) the tetragonal structure is the only phase present. The **Zn-1**⊃$AB_{1.0}$ structure is similar to that of the dimethylformamide-loaded framework (**Zn-1**⊃DMF, Figure 1) which is also contracted due to bending of the linkers. This framework contraction provides an indirect measure of the flexibility of the framework, which is easily quantified using the unit cell parameters derived from XRPD.

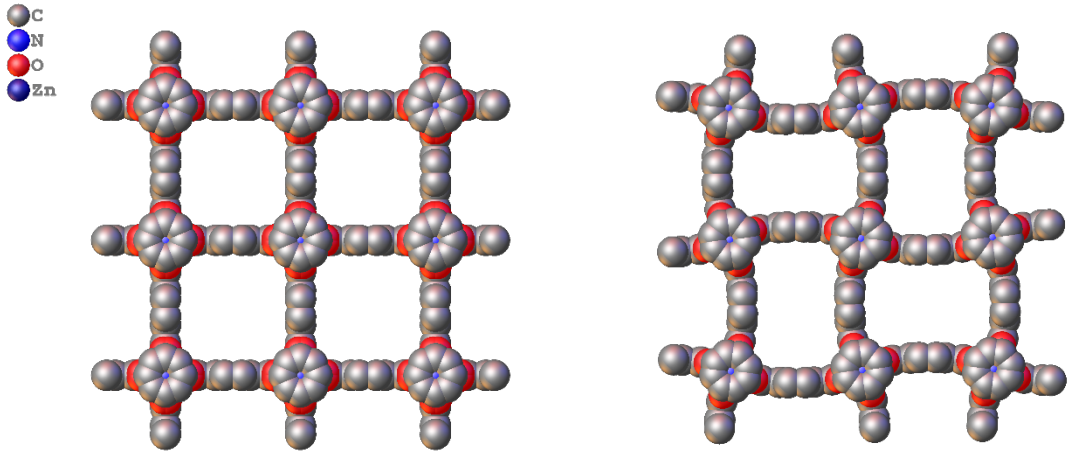

Figure 1. Crystal structure of **Zn-1** (left) and **Zn-1**⊃DMF (right) (CCDC refs: WAFKEU and WAFKAQ) viewed down the c axis with a single layer of paddlewheels shown for simplicity.

Guest DMF molecules and hydrogen atoms are removed for clarity and carbon atoms of the DABCO linker are disordered and shown at ½ occupancy.

It has been shown for paddlewheel MOFs that the metal centre can have a significant influence on the framework flexibility.[40] Klein *et al*. studied the effect of metal ion substitution on the guest-induced flexibility of the pillared $M_2(NDC)_2(DABCO)$ SPCs (M = Co, Ni, Zn; NDC = 2,6-napthalenedicarboxylate).[36] All four samples showed distinct variations of gas adsorption properties and degrees of flexibility as observed by XRPD, which was attributed to the differences in the electronic structures of the metal ions. It was suggested that orbital directing effects of the different electron configurations of the metal ions (Co^{2+} ($3d^7$), Ni^{2+} ($3d^8$), Cu^{2+} ($3d^9$) and Zn^{2+} ($3d^{10}$)) are central to the flexibilities of the analogous composites, in which the breathing effect requires a distortion of the metal coordination sphere away from the ideal square pyramidal geometry. This would be more favourable for a closed shell Zn^{2+} system than the open shell Cu^{2+} system.[41] This was followed by the work of Henke *et al*. on $M_2(BME\text{-}BDC)_2(DABCO)$ (M = Zn, Co, Ni, Cu; BME-BDC = 2,5-bis(2-methoxyethoxy)-1,4-benzenedicarboxylate) which also exhibit structural flexibility and undergo guest- and temperature-induced reversible phase transitions between a narrow pore (*np*) and a large pore (*lp*) form.[42] The *lp* form is structurally analogous with the guest-free **M-1** framework in terms of the space group and unit cell dimensions. These previous studies showed that the *np* ↔ *lp* phase transition enthalpy and transition temperature decrease in the sequence **Zn-1** ≈ **Co-1** > **Ni-1** > **Cu-1**, which correlates with the inherent flexibility of the paddlewheel unit.

To study the influence of the metal ion on the framework contraction of **M-1**⊃AB composites, we prepared a set of samples following the reported loading procedure for **Zn-1**⊃$AB_{1.0}$,[33,37–39] which involves a melt-infiltration procedure of the guest-free framework with excess *trans*-AB.[27] The melt-infiltration is typically followed by a vacuum treatment procedure at 120 ˚C to remove excess *trans*-AB remaining outside the pores.[27] This step is important as the melt-infiltration procedure does not fully saturate **M-1** unless an excess of *trans*-AB is used (Table S1 and Figure S1). Owing to the inherent flexibility of the **M-1** structure, it is possible the vacuum treatment could also change the loading level of the pores and therefore the structural and thermal properties of the composites. To investigate this, **M-1**⊃AB composites were first characterised prior to vacuum treatment (Table 1, Figure S1 and Table S2). These samples are hereafter referred to as **M-1**⊃$AB^{vac\text{-}0h}$.

Table 1. Crystallographic information for guest free frameworks (M-1) and AB-loaded frameworks prior to vacuum treatment (M-1⊃$AB^{vac\text{-}0h}$**).** The degree of contraction refers to the percentage change in reduced unit cell volume as compared to the guest-free *lp* framework.

	Space group	$a = b$ / Å	c / Å	V / Å^3	Guest-induced unit cell contraction (%)	*np* → *op* expansion (%)
Zn-1	*P4/mmm*	10.98	9.65	1164.1	-	
Zn-1⊃$AB^{vac\text{-}0h}$	*I4/mcm*	15.03	19.28	4355.6	6.5	6.1
Co-1	*P4/mmm*	10.98	9.65	1164.1	-	
Co-1⊃$AB^{vac\text{-}0h}$	*I4/mcm*	15.05	19.28	4366.1	6.2	5.5
Ni-1	*P4/mmm*	10.98	9.49	1143.9	-	

Ni-1⊃AB$^{vac\text{-}0h}$	*I4/mcm*	15.23	18.90	4386.5	4.1	1.9
Cu-1	*P4/mmm*	10.91	9.69	1152.9	-	
Cu-1⊃AB$^{vac\text{-}0h}$	*I4/mcm*	15.31	19.35	4535.6	1.7	0.6

Table 1 shows the crystallographic information for **M-1**⊃AB$^{vac\text{-}0h}$ samples derived from profile fitting of XRPD patterns of **M-1** and **M-1**⊃AB$^{vac\text{-}0h}$ (full details of the profile fitting are given in Figure S2-S4). All **M-1**⊃AB$^{vac\text{-}0h}$ conform to the tetragonal space group *I*4/*mcm* previously observed for **Zn-1**⊃AB$_{1.0}$.[27] This indicates that the BDC ligands have distorted due to the contraction of the pore around the occluded *trans*-AB molecules. However, the degree of pore contraction depends upon the nature of the metal ion making up the paddle wheel unit (Table S3). For **Co-1**⊃AB$^{vac\text{-}0h}$, the contraction (6.2%) is comparable to **Zn-1**⊃AB$^{vac\text{-}0h}$ (6.5%). However, **Ni-1**⊃AB$^{vac\text{-}0h}$ undergoes a smaller contraction of 4.1%, consistent with the flexibility of the Ni(II) paddlewheel being lower than Zn(II) and Co(II) analogues. **Cu-1**⊃AB$^{vac\text{-}0h}$ undergoes the smallest contraction of 1.7%. These results are consistent with the structurally analogous M(fu-BDC)$_2$(DABCO) frameworks discussed above,[42] indicating that the orbital directing effects of the metal centres also control the flexibility of **M-1**⊃AB.

To investigate the thermal properties of **M-1**⊃AB$^{vac\text{-}0h}$, cyclic DSC measurements were performed in the range 0 – 200 °C at a rate of 20 °C min^{-1} (Figure 2, Table S2). For the guest-free **M-1** samples, no thermal features were observed in this region, as expected. For each **M-1**⊃AB$^{vac\text{-}0h}$ sample, two transitions are observed on both the heating and cooling branch. The lower temperature features, at approximately 70 °C, are attributed to the melting/crystallisation of excess *trans*-AB (melting point 69 ˚C). The higher temperature features are assigned to a reversible phase

transition which was previously observed for **Zn-1**⊃AB[27] and is reminiscent of the thermally-driven *np* ↔ *lp* phase changes observed for functionalised analogues of **M-1**.[42,43]

Variable-temperature XPRD measurements (Figure S5-S8) confirm the endothermic phase transitions observed in the DSC profiles correspond to a reversible expansion of the **M-1** structure, primarily along the $a = b$ unit cell axes defined by the BDC linkers. For each **M-1**⊃AB$^{vac\text{-}0h}$ sample, profile fitting above the phase transition temperature shows a single phase consistent with the tetragonal *I*4/*mcm* space group (Figure S9). When compared to the ambient-temperature structure, there is a lengthening of the $a = b$ unit cell axis, between 0.8 – 3.2%. However, unlike functionalised analogues of **M-1**, for **M-1**⊃AB$^{vac\text{-}0h}$ above the phase transition the framework does not fully expand to the *lp* dimensions of guest-free **M-1** (Table S4). The fact that the *I*4/*mcm* symmetry is retained suggests the BDC linkers remain bent due to host-guest interactions. Due to this, the structure at temperatures higher than the phase transition will be referred to hereafter as the open-pore (*op*) structure to differentiate from the fully-expanded *lp* structure. The percentage expansion of the unit cell volume appears to be related to the flexibility of the M^{II} paddlewheel and follows the same trend as upon guest loading and the *lp* → *np* contraction. **M-1**⊃AB$^{vac\text{-}0h}$ (M = Zn and Co) show the highest *np* → *op* unit cell expansion of 6.1% and 5.5% respectively, this is followed by **Ni-1**⊃AB$^{vac\text{-}0h}$ at 1.9 % and **Cu-1**⊃AB$^{vac\text{-}0h}$ at 0.6% (Table 1, Table S5).

Table 2. Thermodynamic information for AB-loaded frameworks prior to vacuum treatment (M-1⊃AB$^{vac\text{-}0h}$). Entropies were calculated using the peak temperature of the *np* → *op* endotherm on the first heating branch.

	ΔH / kJ mol^{-1}	T_{peak} / K	ΔS / J K^{-1} mol^{-1}

Zn-1⊃AB$^{vac\text{-}0h}$	27.3	438.9	62.2
Co-1⊃AB$^{vac\text{-}0h}$	27.1	432.6	62.7
Ni-1⊃AB$^{vac\text{-}0h}$	26.8	411.7	65.1
Cu-1⊃AB$^{vac\text{-}0h}$	14.5	376.9	38.5

The mass of excess *trans*-AB in each sample was determined through a calibration curve with crystalline *trans*-AB based on the enthalpy of the melting endotherm (Figure S1) and is shown as a percentage of the total sample mass in Figure 2 (details in Table S2). In each sample, 15-20% of the mass is excess *trans*-AB which suggests similar quantities have been occluded within each **M-1**⊃AB$^{vac\text{-}0h}$ framework. The magnitudes of the *np* → *op* phase transition enthalpies for **M-1**⊃AB$^{vac\text{-}0h}$ (M = Ni, Co, Zn) are similar, ranging between 26.8 – 27.3 kJ mol^{-1}. However, for **Cu-1**⊃AB$^{vac\text{-}0h}$ the enthalpy of 14.5 kJ mol^{-1} is significantly lower. Schneemann *et al*. showed that the onset temperature and magnitude of the *np* ↔ *lp* phase transition enthalpy is related to the degree of contraction of the framework.[42] From the thermodynamic data summarised in Table 2, it can be seen that this trend is followed for the *np* → *op* onset temperature, which reduces from 160 °C (**Zn-1**⊃AB$^{vac\text{-}0h}$ and **Co-1**⊃AB$^{vac\text{-}0h}$) to 133 °C (**Ni-1**⊃AB$^{vac\text{-}0h}$) and 98 °C (**Cu-1**⊃AB$^{vac\text{-}0h}$) in the predicted manner (Zn = Co > Ni > Cu), although the magnitude of the phase transition enthalpy for **Ni-1**⊃AB$_{vac\text{-}0h}$ does not decrease. This may indicate a contribution from framework-guest interactions (*e.g.*, π-π interactions) to the phase transition enthalpy, which are likely to be less significant in alkyl-functionalised analogues.[44–46] The data in Table 2 also shows that for **Ni-1**⊃AB$^{vac\text{-}0h}$, the entropy change associated with the *np* → *op* phase transition is slightly higher than for **Zn-1**⊃AB$^{vac\text{-}0h}$ and **Co-1**⊃AB$^{vac\text{-}0h}$. This could suggest increased ordering of the *trans*-AB molecules within **Ni-1**⊃AB$^{vac\text{-}0h}$ below the phase transition, which may help explain the higher

than expected phase transition enthalpy for this sample. In contrast, the phase transition entropy change for **Cu-1**⊃AB$^{vac\text{-}0h}$ is significantly lower than the other analogues; this is consistent with the lower degree of framework contraction below the phase transition which could impart lower ordering and increased dynamics of the occluded *trans*-AB molecules.

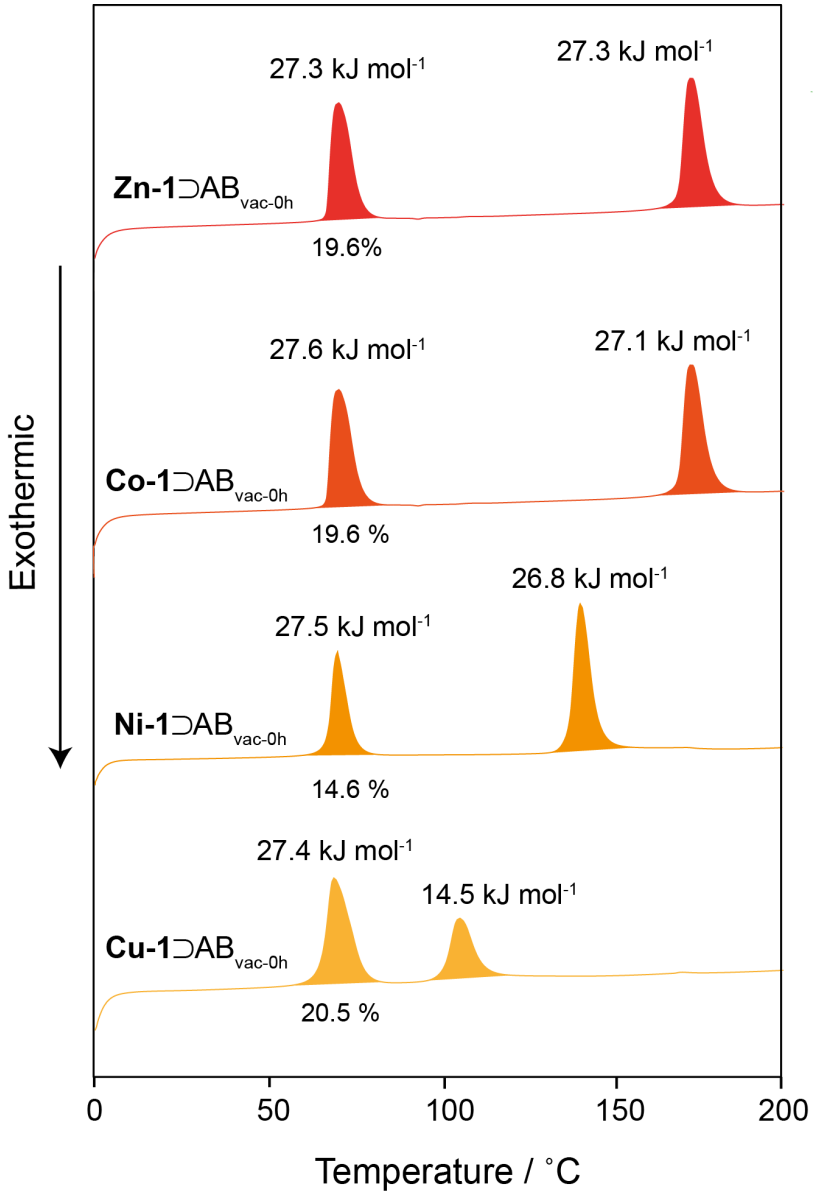

Figure 2. First heating branch of DSC profiles for **M-1**⊃AB$^{vac\text{-}0h}$ between 0 – 200 °C at 20 K min^{-1}. The mass of *trans*-AB as a percentage of the total sample mass is shown below the melting endotherm at 70 °C in each profile.

2.2 Effect of vacuum treatment on the loading level of Zn-1⊃AB

The *np* → *op* phase transition enthalpy of 27.3 kJ mol^{-1} measured for **Zn-1**⊃AB$^{vac\text{-}0h}$ (Figures 2, S3) is significantly higher than the value of 21.6 kJ mol^{-1} obtained in previous work for a sample that was vacuum treated for 3 hours.[27] To investigate the origin of this difference, DSC measurements were carried out on **Zn-1**⊃AB samples that were vacuum treated for between 0 and 6 hours (S18). For each sample, the stoichiometric loading level of the framework was determined from comparison of the excess *trans*-AB melting enthalpy and the ratio of *trans*-AB and **Zn-1** used in the loading procedure. The results (summarised in Figures S10-S14 and Table S6-S8) show that for **Zn-1**⊃AB$^{vac\text{-}0h}$, the framework: occluded *trans*-AB ratio is 1:1.3 corresponding to an estimated pore filling efficiency 78% **Zn-1**⊃AB$_{vac\text{-}0h}$(details in Table S8). This is higher than the previously published composites which had a maximum loading level of 1:1.[32] After 1 hour of vacuum treatment, this ratio reduces to 1:1.1 and the magnitude of the endothermic phase change reduces concomitantly to 24.0 kJ mol^{-1}. Further vacuum treatment reduces the loading level to the previously observed ratio of 1:1 and the endothermic phase change enthalpy reduces further to 21.6 kJ mol^{-1}, similar to the value observed in the previous work. Between 2 – 5 hours of vacuum treatment, no further change the loading level or phase transition enthalpy is observed, but after 6 hours the loading level and phase transition enthalpy reduce. XRPD patterns (Figures S12-S13) and ^{13}C CPMAS NMR spectra (Figure S14) recorded between 0 – 6 hours of vacuum treatment

show no evidence of structural changes in the framework although loss of excess *trans*-AB is observed.

The DSC and structural measurements show that the loading level of the **Zn-1** framework is sensitive to the duration of vacuum treatment. Between 2 - 5 h of treatment, the excess *trans*-AB is fully removed and the loading level stabilises at a composition of **Zn-1**⊃$AB_{1.0}$ in the tetragonal *np* structure, as was observed previously.[27] However, further vacuum treatment removes *trans*-AB from the framework and the structure changes to the orthorhombic *np* structure. Interestingly, for short vacuum treatment times, higher loading levels are observed, with a maximum composition of **Zn-1**⊃$AB_{1.3}$. This is only observed while excess *trans*-AB remains outside the pores, which, at the *np* → *op* phase transition temperature, should form a liquid reservoir surrounding the **Zn-1**⊃AB particles. The reservoir appears to stabilise higher occupancy of the framework by *trans*-AB. As the excess is removed by vacuum treatment, the reservoir no longer surrounds some particulates and, in these regions, *trans*-AB is removed from the pores until it is stable at a loading level of **Zn-1**⊃$AB_{1.0}$. A recent study by Rodl and co-workers showed that similarly-sized *ortho*-tetrafluoroazobenzene (tf-AB) can be loaded into **Zn-1** to a maximum loading of 1.5 tf-AB per formula unit.[47] However, the observed space group is not tetragonal and is instead orthorhombic and similar to that observed by Yanai *et al*.[32] These results suggest that the maximum loading level of the framework depends upon a number of factors including the chemical and structural properties of the guest, the presence of excess guest molecules outside the framework, and the structural change of the framework resulting from guest-induced breathing.

2.3 Thermal properties of M-1⊃AB (M = Zn, Co, Ni, Cu) composites

To perform a systematic comparison of the thermal properties, samples of **M-1**⊃AB (M = Zn, Co, Ni) were vacuum treated for 3 h to remove excess *trans*-AB but to maintain a defined composition of **M-1**⊃$AB_{1.0}$. Compositions of all samples were confirmed by both TGA (Figure S15) and UV-vis spectroscopy quantification on solvent-extracted samples (Figure S16 and Table S9). The XRPD patterns of the vacuum-treated **M-1**⊃$AB_{1.0}$ (M = Zn, Co, Ni) are consistent with the tetragonal *I*4/*mcm* space group and unit cell dimensions of the **M-1**⊃$AB^{vac\text{-}0h}$ composites. (Figure S17). However, for **Cu-1**⊃AB, vacuum treatment for 3 h led to the emergence of XRPD reflections consistent with the tetragonal *P*4/*mmm* space group, suggesting that *trans*-AB was removed from the pores. This is consistent with the lower degree of contraction for **Cu-1**⊃$AB^{vac\text{-}0h}$ meaning the *trans*-AB molecules are less confined within the pores. Even with shorter vacuum treatment times (0.5 - 2 h) and lower vacuum treatment temperatures below the *np* → *op* phase transition temperature (80 – 90 °C), loss of *trans*-AB from the pores of **Cu-1**⊃AB was still observed (Figure S18). Therefore, in order to maximise the loading of **Cu-1**, samples were loaded with increasing amounts of *trans*-AB without vacuum treatment. This resulted in four composites with different loading levels (described in Figure S19). The highest loading level without excess *trans*-AB was **Cu-1**⊃$AB_{0.9}$. DSC measurements for the **Cu-1**⊃AB_x (x = 0.2 – 0.9) series show a reversible phase transition for which the onset temperature and enthalpy increase linearly with the loading level.

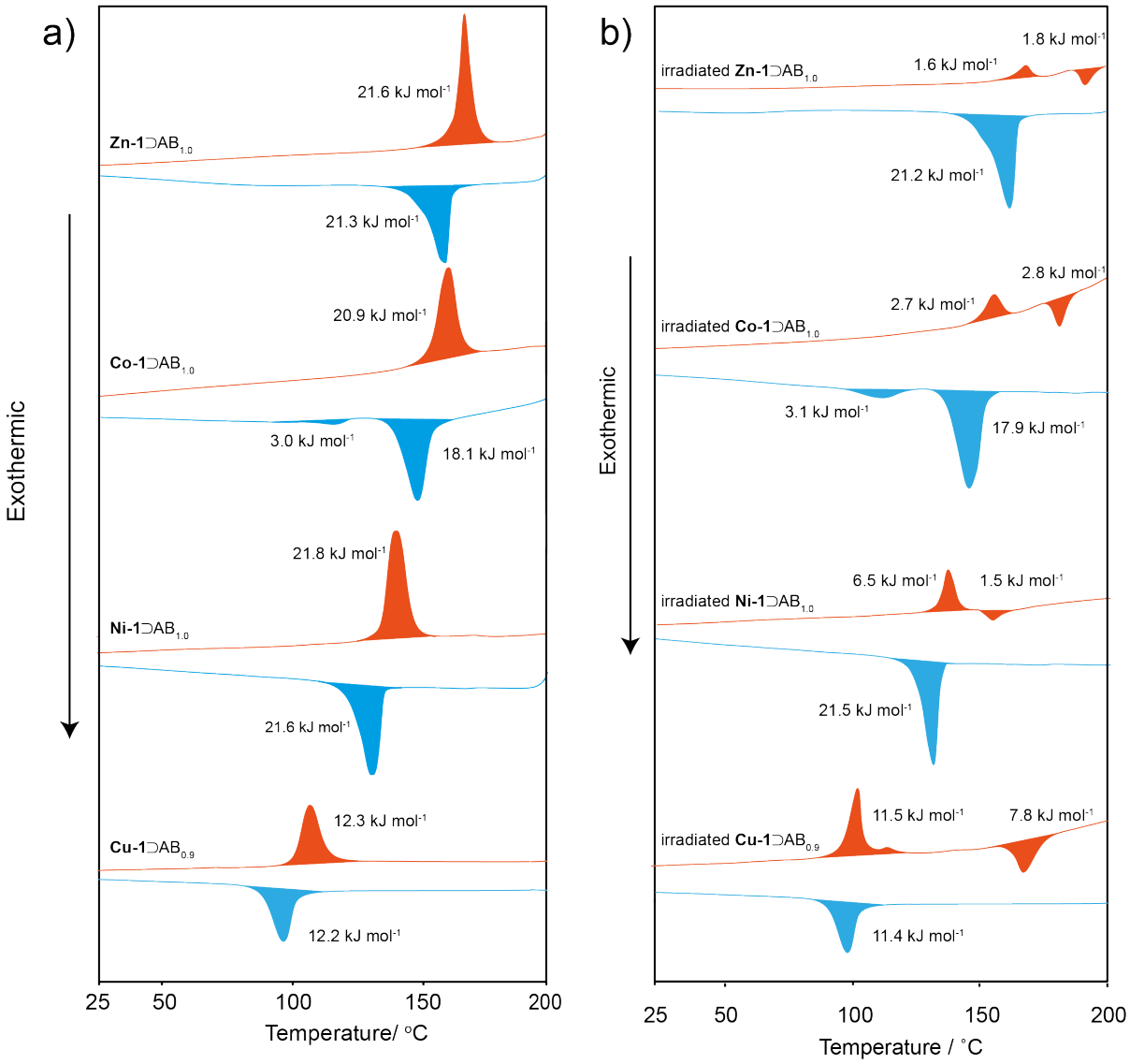

Figure 3. (a) First heating cycle of DSC studies for **M-1**⊃$AB_{1.0}$ (**M** = Zn, Co, Ni) and **Cu-1**⊃$AB_{0.9}$ between 0 – 200 °C. (b) First heating cycle of DSC studies for irradiated **M-1**⊃$AB_{1.0}$ (**M** = Zn, Co, Ni) and **Cu-1**⊃$AB_{0.9}$ between 0 – 200 °C.

DSC profiles for **M-1**⊃$AB_{1.0}$ (**M** = Zn, Co, Ni) and **Cu-1**⊃$AB_{0.9}$ are shown in Figure 3. The thermal features for **Zn-1**⊃$AB_{1.0}$ are identical to those previously reported.1 For **Co-1**⊃$AB_{1.0,}$ the *np* → *op* transition on the heating branch onsets at 159.4 °C, with an enthalpy of 20.9 kJ mol^{-1}, while two *op* → *np* transitions are observed on the cooling branch at 147.7 °C, and 115.9 °C with enthalpies of 18.1 kJ mol^{-1} and 3.0 kJ mol^{-1}, respectively. It is possible that the **Co-1** framework has a higher proportion of defects that create a local heterogeneity leading to the second lower energy *op* → *np* transition. Interestingly, a similar two-component exotherm arising from the same pore closing process was previously observed in functionalised Co(fu-BDC)$_2$(DABCO).[48] For **Ni-1**⊃$AB^{vac\text{-}3h}$, the *np* ↔ *op* transition has a similar enthalpy although the onset temperatures during heating and cooling are more than 20 °C lower than **Co-1**⊃$AB_{1.0}$ and **Zn-1**⊃$AB_{1.0}$. For **Cu-1**⊃$AB_{0.9}$, the magnitude and onset temperature of *np* ↔ *op* endotherm is the lowest of the **M-1**⊃AB_x samples with values of 104 °C and 12.3 kJ mol^{-1} respectively (Figure 3). This is of a similar magnitude to that observed in **Cu-1**⊃$AB^{vac\text{-}0h}$, suggesting that the loading level in both samples is similar.

Yanai *et al*. showed that *trans*-AB guest molecules in **Zn-1**⊃AB_x exhibit photoisomerisation to the metastable *cis* isomer upon exposure to UV light, which in turn, induces a structural change to the host framework.[32] To determine how the flexibility of the M(II) paddlewheels affects the isomerisation of AB in the **M-1** pores, **M-1**⊃$AB_{1.0}$ (M = Zn, Co, Ni) and **Cu-1**⊃$AB_{0.9}$ was irradiated with 365 nm light for up to 9 hours. Subsequent solvent extraction of the guest AB molecules followed by ^{1}H NMR showed that photoisomerisation to *cis*-AB takes place within all **M-1**⊃AB_x composites (Figure S20). However, the population of *cis*-AB at the photostationary state (PSS) and the photoisomerisation kinetics both appear to be dependent on the nature of the M(II) paddlewheel unit and initial degree of contraction of the framework (Figure 4a, Figures S21-

S22 and Table S10). **Zn-1**⊃$AB_{1.0}$ and **Co-1**⊃$AB_{1.0}$ both reach a PSS of 38-40% *cis*-AB after 300 minutes of irradiation, whereas **Ni-1**⊃$AB_{1.0}$ reaches a lower PSS of 33% after 360 minutes, and **Cu-1**⊃$AB_{0.9}$ reaches a PSS of only 15% after 560 minutes. The PSS is approximately linearly related to the degree of *lp* → *np* contraction observed when the guest-free framework is initially loaded with *trans*-AB (Figure 4b). This suggests that greater MOF flexibility allows for a higher degree of guest rearrangement upon isomerisation.

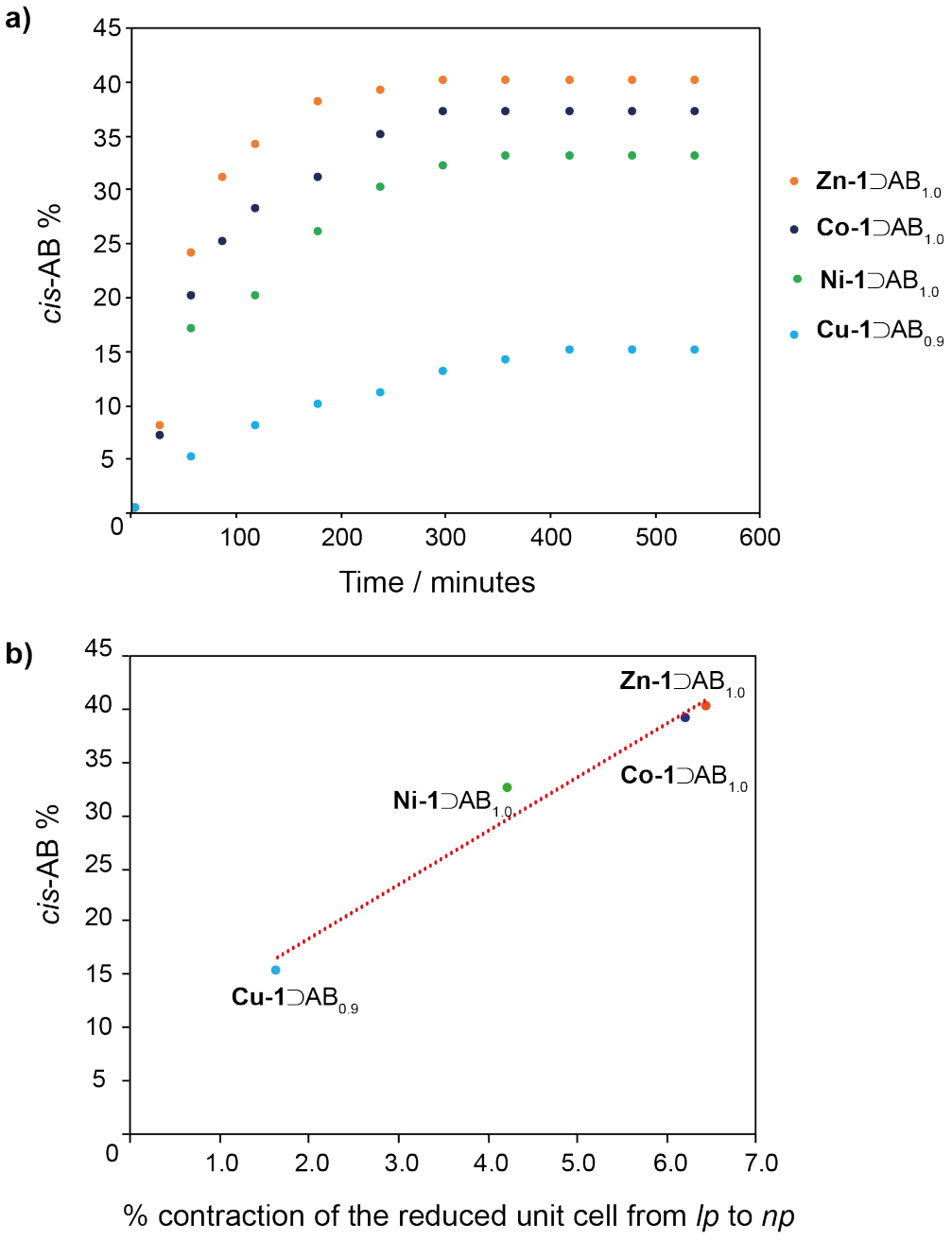

Figure 4. (a) The proportion of *cis*-AB in **M-1**⊃AB_x as a function of irradiation time as measured by ^{1}H NMR. (b) The proportion of *cis*-AB in **M-1**⊃AB_x at the PSS as a function of the degree of *lp* → *np* contraction of **M-1**⊃AB_x upon loading framework with *trans*-AB.

XRPD measurements for **M-1**⊃$AB_{1.0}$ (M = Zn, Co, Ni) and **Cu-1**⊃$AB_{0.9}$ show a slight shifting of the tetragonal *np* reflections and emergence of new reflections with increasing UV irradiation time. As the fraction of *cis*-AB increases, the relative intensities of the new reflections also increase and dominate the pattern. For each sample, the reflections for the new phases were extracted and Le Bail fitting analyses showed good agreement with the same tetragonal space group *I4/mcm* (Figure S23 and Table S11). However, in each case longer $a = b$ unit cell lengths were observed, whereas the c unit cell length remained almost constant (Table S12). The increase of the $a = b$ unit cell lengths resulted in respective unit cell volume expansions of 5.2%, 4.7% and 3.2% for **M-1**⊃$AB_{1.0}$ (M = Zn, Co, Ni) and 1.2% for **Cu-1**⊃$AB_{0.9}$. Irradiation-induced unit cell volume changes are visually represented in Figure 5 which compares them with the guest-induced *lp* → *np* contraction and the thermally-driven expansion at the *np* → *op* phase transition. In each case, the expansion of the unit cell due to UV irradiation is remains 1 - 2% smaller than the guest-free *lp* structure. Interestingly, for **Ni-1**⊃$AB_{1.0}$ and **Cu-1**⊃$AB_{0.9}$, the irradiation-induced expansion is larger than the expansion at the *np* → *op* phase transition. This may indicate that *cis*-AB molecules within these composites are in highly strained local environments. For **Co-1**⊃$AB_{1.0}$ and **Zn-1**⊃$AB_{1.0}$, XPRD shows the *np* phase is not present at the PSS (Figure S23). This supports previous observations that the structural change is global and does not occur in domains or suffer from UV light penetration effects[32] – *i.e.*, at the PSS the *cis*-AB and *trans*-AB molecules are present within the same phase. Indeed, diffuse reflectance UV-vis spectra of the **M-1** frameworks (Figure S24) and pure *trans*-AB (Figure S25) show that while there is some overlap in absorption at 365 nm, this does not correlate with the PSS of the composites.

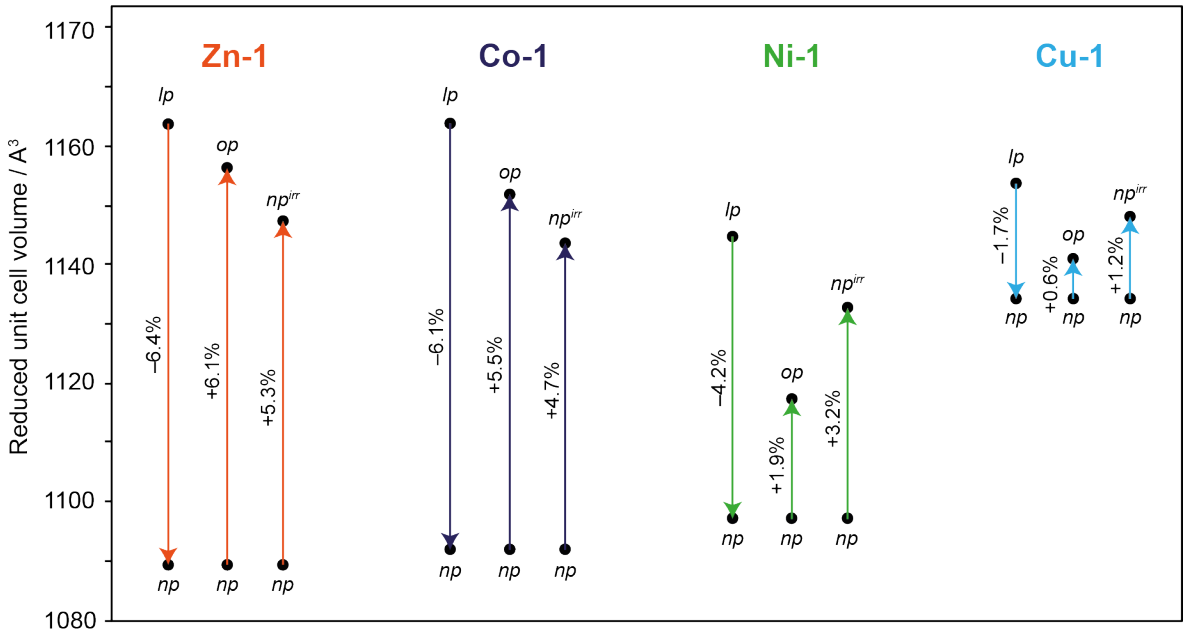

Figure 5. Scheme to display the relative contraction and expansion of the reduced unit cell volume of **M-1** in this study. These highlight the effects of guest occlusion (*lp* → *np*), temperature-induced phase transition (*np* → *op*) and irradiation with 365 nm light (*np* → *np*^{irr}).

Figure 3b shows DSC profiles for **M-1**⊃$AB_{1.0}$ (M = Zn, Co, Ni) and **Cu-1**⊃$AB_{0.9}$ after 300 minutes of UV irradiation. Full thermal data is presented in Figures S26-S29 and Tables S13-S17. In the first heating cycle, much smaller features are observed for **M-1**⊃$AB_{1.0}$ (M = Zn, Co, Ni); this was seen previously for **Zn-1**⊃$AB_{1.0}$ and experiments at different *cis*-AB populations showed that this originates from almost complete cancelling of the *np* → *op* endotherm by an exotherm due to thermal reconversion of *cis*-AB to *trans*-AB.[27] Indeed, based on the DFT-calculated energy difference of 52 kJ mol^{-1} between *cis*- and *trans*-AB (Table S18), a PSS of 40% should result in an exotherm of 21 kJ mol^{-1} upon thermal reconversion. This is very close to the magnitude of the *np* → *op* endotherm in both **Zn-1**⊃$AB_{1.0}$ and **Co-1**⊃$AB_{1.0}$. For irradiation **Ni-1**⊃$AB_{1.0}$, the residual endotherm is significantly higher (6.5 kJ mol^{-1}) than the Zn and Co analogues; this is consistent

with the lower PSS in this sample (33%) meaning that the thermal reconversion exotherm does not cancel the phase transition endotherm (Table S19-S21). On the first cooling branches, the *op* → *np* transition energies and onset temperature are identical to the non-irradiated samples. For all composites a further heating/cooling cycles are the same as the non-irradiated form. This confirms that the 0 – 200 °C thermal cycle causes full reconversion of the occluded *cis*-AB to *trans*-AB. Moreover, the absence of exothermic features below the *np* → *op* phase transition temperatures suggest that the *cis* → *trans* reconversion may be linked to the pore opening at the phase transition.

The thermal behaviour of irradiated **Cu-1**⊃$AB_{0.9}$ is distinct when compared to the other examples. The endothermic and exothermic features on the first heating branch are separated by ~50 ˚C and throughout the 9-hour irradiation time the endothermic feature only decreases by 0.8 kJ mol^{-1} (Figure S29a). The exothermic feature emerges after one hour of irradiation, and the magnitude increases with irradiation time before plateauing at between 8 – 9 hours at 7.9 kJ mol^{-1} (Figure S29c). The maximum population of *cis*-AB at the PSS for this sample is 15% (Figure 4a), and the theoretical enthalpy for *cis* → *trans* reconversion of this proportion (7.8 kJ mol^{-1}) corresponds well with the observed exotherm (Table S21). Therefore, the exothermic feature on the heating step can be attributed to thermal *cis* → *trans* reconversion of the occluded AB molecules, although unlike the other metal analogues, this does not appear to be coincident with the endothermic transition. Instead, the thermal reconversion takes place at a significantly higher temperature (160 °C), suggesting a significantly increased activation energy barrier. This is surprising given the lower degree of contraction of this framework and the increased mobility of the occluded AB molecules that is evident from the propensity to leave the pores during vacuum treatment. One possibility is that the local ordering of the *cis*-AB molecules within the pores differs

significantly from the other composites; indeed this may be related to the large irradiation-induced unit cell expansion (Figure 5). The XRPD pattern of irradiated **Cu-1**⊃$AB_{0.9}$ recorded at 120 °C shows that above the phase transition, but before the reconversion of *cis*-AB to *trans*-AB, the framework adopts the *lp* structure (Figures S30-S31). This contrasts the unirradiated composite where the slightly contracted *op* structure is observed above the phase transition. However, the precise local structure is not clear from XRPD and solid-state NMR measurements are complicated by paramagnetic interactions from the Cu^{2+} ions. Further work is required to fully understand the structural and thermal properties of this specific system.

2.4 Energy Storage properties of M-1⊃$AB_{1.0}$ composites

The thermally-induced reversible phase transition observed for the **M-1**⊃AB system gives it the properties of a ss-PCM where thermal energy can be stored above the *np* → *op* phase transition, and recovered through reversal of the phase transition upon cooling. For the irradiated composites, energy is stored within the metastable *cis*-AB molecule, giving the composite the properties of a hybrid STF and ss-PCM. The exotherm associated with thermally-driven reconversion of *cis*-AB to *trans*-AB during heating is comparable in magnitude to the phase transition endotherm, meaning that the net heat flow during the heating step is negligible. However, at the end of the heating branch, the *cis*-AB molecules have thermally relaxed to *trans*-AB. The material now has the structural properties of non-irradiated **M-1**⊃$AB_{1.0}$ in the *op* structure, and therefore the exothermic phase transition is observed on the cooling branch. This means that over one full heating and cooling cycle there is a net energy output of 28.9 J g^{-1} for **Zn-1**⊃$AB_{1.0}$, 28.0 J g^{-1} for **Co-1**⊃$AB_{1.0}$ and 22.9 J g^{-1} for **Ni-1**⊃$AB_{1.0}$ and 11.5 J g^{-1} for **Cu-1**⊃$AB_{0.9}$ (Figure S32).

The gravimetric energy densities of the composites are modest compared to other ss-PCM and STF architectures. Templated azobenzene derivatives have been reported with energy densities between 90-200 J g^{-1},[22,49] while organic ss-PCMs can store in excess of 100 J g^{-1},[5] and organometallic ss-PCMs show energy densities in the range of 60–165 J g^{-1}.[5] However, it should be possible to increase the energy density of MOF-AB composites if higher loading levels can be stabilised either by functionalising the MOF or AB structure, or by using larger-pore MOFs which can accommodate a higher proportion of AB. Furthermore, a key limitation in the current composites is the PSS which reaches a maximum of 40% for **Zn-1**⊃$AB_{1.0}$. The PSS appears to be dependent upon the degree of framework flexibility and further refinement of this may lead to higher PSSs which in principle could increase the energy density by more than a factor of two.

In addition to the energy density, another important property of STFs is the duration for which energy can be stored under ambient conditions. For polymer and molecular azobenzene-based STFs, the half-lives of *cis*-AB isomeric states are typically on the order of tens of hours in the solid-state, making these materials useful for *e.g.*, daily repeat cycle applications.

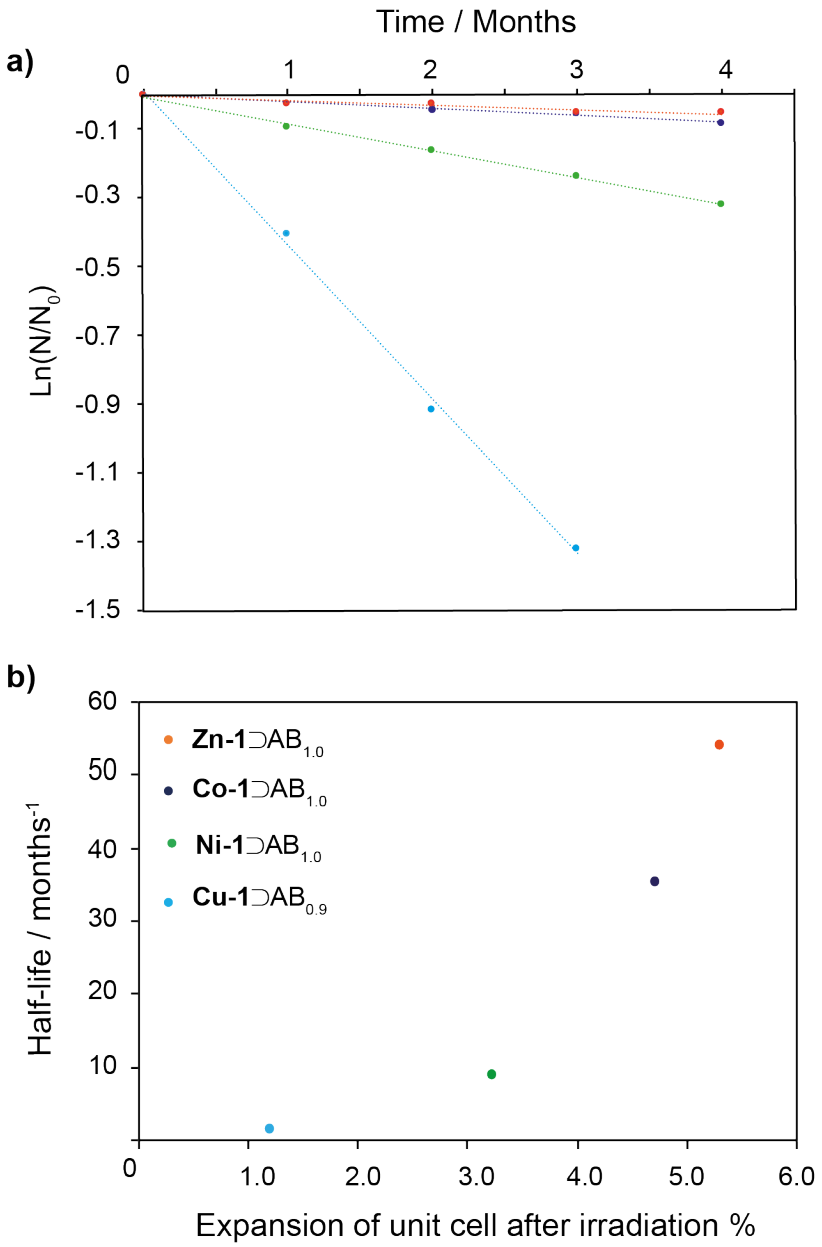

Figure 6. (a) Logarithmic plot of the normalised population of *cis*-AB occluded within irradiated **M-1**⊃$AB_{1.0}$ composites at ambient temperature in the dark as a function of time. b) Plot of *cis*-AB half-lives within irradiated **M-1**⊃$AB_{1.0}$ composites as a function of the percentage unit cell expansion upon irradiation.

To estimate the half-lives of *cis*-AB in the **M-1**⊃AB composites, irradiated samples were kept in the dark at 25 ˚C for four months, with portions extracted and quantified at regular intervals (Tables S22-S23). Figure 6a shows that spontaneous thermal reconversion follows first-order Arrhenius kinetics which is expected for these systems. Linear fits to the data give *cis*-AB half-lives of 4.5 years for **Zn-1**⊃$AB_{1.0}$ 3.0 years for **Co-1**⊃$AB_{1.0}$, 9 months for **Ni-1**⊃$AB_{1.0}$, and 1.5 months for **Cu-1**⊃$AB_{1.0.}$ The half-life of *cis*-AB in solution at ambient temperature is on the order of 100 hours.[50]

These results demonstrate that confinement can significantly increase the lifetime of the metastable isomer. Furthermore, the *cis*-AB half-life appears to be linked to the structural changes that take place upon photoisomerization of the guest molecules. In Figure 6b it can be clearly seen that frameworks which undergo larger unit cell expansions upon irradiation exhibit significantly longer *cis*-AB half-lives. This indicates that framework flexibility, and the ability of the pores to contract around the guest molecules plays a role in "trapping" the *cis* isomer and thereby imposing a higher activation energy barrier for reconversion to the ground-state *trans* isomer. This effect could be exploited to develop materials for long term (*e.g.*, seasonal) energy storage.

3. CONCLUSION

The nature of the metal ion in $M(BDC)_2(DABCO)AB_x$ (**M-1**⊃AB_x; M = Zn, Co, Ni, Cu) composites directly affects the breathing behaviour and the thermal properties of these materials. For all frameworks studied, loading of the pores with *trans*-AB is accompanied by a guest-induced contraction of the unit cell, the extent of which is linked to the inherent flexibility of the M(II) paddlewheel unit. The magnitude of the guest-induced unit cell contraction decreases in the order **Zn-1** ≈ **Co-1** > **Ni-1** > **Cu-1** which is consistent with previous observations for structurally similar

systems. Upon heating, all composites display a reversible *np* → *op* phase transition, although the *op* structure remains partially contracted relative to the guest-free *lp* structure. The magnitude of the unit cell expansion at the *np* → *op* phase transition follows the same pattern as the guest-induced unit cell contraction, suggesting that this is also regulated by the intrinsic flexibility of the framework. The enthalpy of the *np* → *op* phase transition is directly proportional to the *trans*-AB loading level and is linked to the flexibility of the framework, although host-guest interactions and entropic effects may also be relevant.

M-1⊃AB (M = Zn, Co, Ni) can be loaded with an excess of guest to a loading level of 1.3 *trans*-AB molecules per framework formula unit. Subsequent vacuum treatment removes excess *trans*-AB from outside the pores, but simultaneously removes molecules from inside the pores to a stable loading level of **M-1**⊃$AB_{1.0}$. In contrast, the rigidity of Cu paddlewheels sees rapid dissociation of *trans*-AB from the framework during vacuum treatment, and this MOF must be accurately loaded to prevent an excess.

UV irradiation of **M-1**⊃$AB_{1.0}$ causes photoisomerization of the occluded *trans*-AB molecules to the metastable *cis* isomer. The population of *cis*-AB at the photostationary state is linked to the flexibility of the framework structure, with the more flexible **Zn-1** and **Co-1** frameworks giving the highest photostationary states. For **M-1**⊃$AB_{1.0}$ (M = Zn, Co, Ni), the energy stored within the occluded *cis*-AB molecules can be retrieved indirectly via the exothermic *op* → *np* phase transition within a full heating-cooling cycle. In contrast, **Cu-1**⊃$AB_{1.0}$ shows distinct thermal properties where the *cis* → *trans* reconversion exotherm is directly observed above the phase transition temperature. Another finding of this work is that confinement within the MOF framework

significantly increases the thermal stability of *cis*-AB compared to the solution state, resulting in half-lives of up to several years at ambient temperature. These findings imply that the pursuit of more efficient photoswitching in MOFs should focus on highly flexible scaffolds.

ASSOCIATED CONTENT

The Supporting Information is available free of charge at XXX.

Synthesis procedures, XRPD, TGA, UV-vis data, Thermal and Irradiation data.

AUTHOR INFORMATION

Corresponding Author

*Dr John M. Griffin, email j.griffin@lancaster.ac.uk

Authors

The manuscript was written through contributions of all authors. All authors have given approval to the final version of the manuscript.

Funding Sources

Leverhulme Trust (Research Project Grant Number RPG-2018-395).

ACKNOWLEDGMENT

We are grateful to the Leverhulme Trust for funding this project.

4. REFERENCES

(1) Yuan, K.; Shi, J.; Aftab, W.; Qin, M.; Usman, A.; Zhou, F.; Lv, Y.; Gao, S.; Zou, R. Engineering the Thermal Conductivity of Functional Phase-Change Materials for Heat Energy Conversion, Storage, and Utilization. *Adv. Funct. Mater.* **2020**, *30* (8), 1–31.

https://doi.org/10.1002/adfm.201904228.

(2) Umair, M. M.; Zhang, Y.; Iqbal, K.; Zhang, S.; Tang, B. Novel Strategies and Supporting Materials Applied to Shape-Stabilize Organic Phase Change Materials for Thermal Energy Storage–A Review. *Appl. Energy* **2019**, *235* (October 2018), 846–873. https://doi.org/10.1016/j.apenergy.2018.11.017.

(3) Alkan, C.; Günther, E.; Hiebler, S.; Ensari, Ö. F.; Kahraman, D. Polyurethanes as Solid-Solid Phase Change Materials for Thermal Energy Storage. *Sol. Energy* **2012**, *86* (6), 1761–1769. https://doi.org/10.1016/j.solener.2012.03.012.

(4) Jiang, Y.; Liu, M.; Sun, Y. Review on the Development of High Temperature Phase Change Material Composites for Solar Thermal Energy Storage. *Sol. Energy Mater. Sol. Cells* **2019**, *203* (July), 110164. https://doi.org/10.1016/j.solmat.2019.110164.

(5) Fallahi, A.; Guldentops, G.; Tao, M.; Granados-Focil, S.; Van Dessel, S. Review on Solid-Solid Phase Change Materials for Thermal Energy Storage: Molecular Structure and Thermal Properties. *Appl. Therm. Eng.* **2017**, *127*, 1427–1441. https://doi.org/https://doi.org/10.1016/j.applthermaleng.2017.08.161.

(6) Zalba, B.; Marín, J. M.; Cabeza, L. F.; Mehling, H. Review on Thermal Energy Storage with Phase Change: Materials, Heat Transfer Analysis and Applications. *Applied Thermal Engineering*. 2003. https://doi.org/10.1016/S1359-4311(02)00192-8.

(7) Mofijur, M.; Mahlia, T. M. I.; Silitonga, A. S.; Ong, H. C.; Silakhori, M.; Hasan, M. H.; Putra, N.; Ashrafur Rahman, S. M. Phase Change Materials (PCM) for Solar Energy Usages and Storage: An Overview. *Energies* **2019**, *12* (16), 1–20.

https://doi.org/10.3390/en12163167.

(8) Chen, X.; Gao, H.; Tang, Z.; Wang, G. Metal-Organic Framework-Based Phase Change Materials for Thermal Energy Storage. *Cell Reports Physical Science*. 2020. https://doi.org/10.1016/j.xcrp.2020.100218.

(9) Tokoro, H.; Yoshikiyo, M.; Imoto, K.; Namai, A.; Nasu, T.; Nakagawa, K.; Ozaki, N.; Hakoe, F.; Tanaka, K.; Chiba, K.; Makiura, R.; Prassides, K.; Ohkoshi, S. I. External Stimulation-Controllable Heat-Storage Ceramics. *Nat. Commun.* **2015**. https://doi.org/10.1038/ncomms8037.

(10) Han, G. G. D.; Li, H.; Grossman, J. C. Optically-Controlled Long-Term Storage and Release of Thermal Energy in Phase-Change Materials. *Nat. Commun.* **2017**. https://doi.org/10.1038/s41467-017-01608-y.

(11) Han, G. G. D.; Deru, J. H.; Cho, E. N.; Grossman, J. C. Optically-Regulated Thermal Energy Storage in Diverse Organic Phase-Change Materials. *Chem. Commun.* **2018**, *54* (76), 10722–10725. https://doi.org/10.1039/C8CC05919E.

(12) Sundararajan, S.; Samui, A. B.; Kulkarni, P. S. Versatility of Polyethylene Glycol (PEG) in Designing Solid-Solid Phase Change Materials (PCMs) for Thermal Management and Their Application to Innovative Technologies. *J. Mater. Chem. A* **2017**, *5* (35), 18379–18396. https://doi.org/10.1039/c7ta04968d.

(13) Kucharski, T. J.; Tian, Y.; Akbulatov, S.; Boulatov, R. Chemical Solutions for the Closed-Cycle Storage of Solar Energy. *Energy Environ. Sci.* **2011**, *4* (11), 4449–4472. https://doi.org/10.1039/c1ee01861b.

(14) Dong, L.; Feng, Y.; Wang, L.; Feng, W. Azobenzene-Based Solar Thermal Fuels: Design, Properties, and Applications. *Chem. Soc. Rev.* **2018**, *47* (19), 7339–7368. https://doi.org/10.1039/c8cs00470f.

(15) Mansø, M.; Petersen, A. U.; Wang, Z.; Erhart, P.; Nielsen, M. B.; Moth-Poulsen, K. Molecular Solar Thermal Energy Storage in Photoswitch Oligomers Increases Energy Densities and Storage Times. *Nat. Commun.* **2018**, *9* (1), 1–7. https://doi.org/10.1038/s41467-018-04230-8.

(16) Wang, Z.; Roffey, A.; Losantos, R.; Lennartson, A.; Jevric, M.; Petersen, A. U.; Quant, M.; Dreos, A.; Wen, X.; Sampedro, D.; Börjesson, K.; Moth-Poulsen, K. Macroscopic Heat Release in a Molecular Solar Thermal Energy Storage System. *Energy Environ. Sci.* **2019**, *12* (1), 187–193. https://doi.org/10.1039/c8ee01011k.

(17) Wu, S.; Butt, H. J. Solar-Thermal Energy Conversion and Storage Using Photoresponsive Azobenzene-Containing Polymers. *Macromol. Rapid Commun.* **2020**, *41* (1). https://doi.org/10.1002/marc.201900413.

(18) Wang, Z.; Losantos, R.; Sampedro, D.; Morikawa, M. A.; Börjesson, K.; Kimizuka, N.; Moth-Poulsen, K. Demonstration of an Azobenzene Derivative Based Solar Thermal Energy Storage System. *J. Mater. Chem. A* **2019**, *7* (25), 15042–15047. https://doi.org/10.1039/c9ta04905c.

(19) Dreos, A.; Wang, Z.; Udmark, J.; Ström, A.; Erhart, P.; Börjesson, K.; Nielsen, M. B.; Moth-Poulsen, K. Liquid Norbornadiene Photoswitches for Solar Energy Storage. *Adv. Energy Mater.* **2018**, *8* (18), 1–9. https://doi.org/10.1002/aenm.201703401.

(20) Gerkman, M. A.; Gibson, R. S. L.; Calbo, J.; Shi, Y.; Fuchter, M. J.; Han, G. G. D. Arylazopyrazoles for Long-Term Thermal Energy Storage and Optically-Triggered Heat Release below 0 °C. *J. Am. Chem. Soc.* **2020**. https://doi.org/10.1021/jacs.0c00374.

(21) Kolpak, A. M.; Grossman, J. C. Azobenzene-Functionalized Carbon Nanotubes as High-Energy Density Solar Thermal Fuels. *Nano Lett.* **2011**, *11*, 3156–3162. https://doi.org/10.1021/nl201357n.

(22) Zhitomirsky, D.; Cho, E.; Grossman, J. C. Solid-State Solar Thermal Fuels for Heat Release Applications. *Adv. Energy Mater.* **2016**, *6* (6), 1502006. https://doi.org/doi:10.1002/aenm.201502006.

(23) Cho, E. N.; Zhitomirsky, D.; Han, G. G. D.; Liu, Y.; Grossman, J. C. Molecularly Engineered Azobenzene Derivatives for High Energy Density Solid-State Solar Thermal Fuels. *ACS Appl. Mater. Interfaces* **2017**, *9* (10), 8679–8687. https://doi.org/10.1021/acsami.6b15018.

(24) Zhao, R.; Zhang, Y.; Mu, J.; Yu, C.; Pan, Y.; Zhao, J.; Wang, Q.; Zhang, S.; Yang, B.; Liu, F. Preparation of Photoresponsive Film via Electrodeposition Approach for Ready-to-Use Solar Thermal Fuel Device. *Adv. Mater. Interfaces* **2020**. https://doi.org/10.1002/admi.202001079.

(25) Hu, J.; Huang, S.; Yu, M.; Yu, H. Flexible Solar Thermal Fuel Devices: Composites of Fabric and a Photoliquefiable Azobenzene Derivative. *Adv. Energy Mater.* **2019**. https://doi.org/10.1002/aenm.201901363.

(26) Liu, Y.; Grossman, J. C. Accelerating the Design of Solar Thermal Fuel Materials through

High Throughput Simulations. *Nano Lett.* **2014**, *14* (12), 7046–7050. https://doi.org/10.1021/nl5034073.

(27) Griffiths, K.; Halcovitch, N. R.; Griffin, J. M. Long-Term Solar Energy Storage under Ambient Conditions in a MOF-Based Solid-Solid Phase-Change Material. *Chem. Mater.* **2020**. https://doi.org/10.1021/acs.chemmater.0c02708.

(28) Dybtsev, D. N.; Chun, H.; Kim, K. Rigid and Flexible: A Highly Porous Metal-Organic Framework with Unusual Guest-Dependent Dynamic Behavior. *Angew. Chemie - Int. Ed.* **2004**. https://doi.org/10.1002/anie.200460712.

(29) Hungerford, J.; Walton, K. S. Room-Temperature Synthesis of Metal-Organic Framework Isomers in the Tetragonal and Kagome Crystal Structure. *Inorg. Chem.* **2019**. https://doi.org/10.1021/acs.inorgchem.8b03202.

(30) Kim, Y.; Haldar, R.; Kim, H.; Koo, J.; Kim, K. The Guest-Dependent Thermal Response of the Flexible MOF Zn2(BDC)2(DABCO). *Dalt. Trans.* **2016**, *45* (10), 4187–4192. https://doi.org/10.1039/c5dt03710g.

(31) Grosch, J. S.; Paesani, F. Molecular-Level Characterization of the Breathing Behavior of the Jungle-Gym-Type DMOF-1 Metal-Organic Framework. *J. Am. Chem. Soc.* **2012**, *134* (9), 4207–4215. https://doi.org/10.1021/ja2100615.

(32) Yanai, N.; Uemura, T.; Inoue, M.; Matsuda, R.; Fukushima, T.; Tsujimoto, M.; Isoda, S.; Kitagawa, S. Guest-to-Host Transmission of Structural Changes for Stimuli-Responsive Adsorption Property. *J. Am. Chem. Soc.* **2012**, *134* (10), 4501–4504. https://doi.org/10.1021/ja2115713.

(33) Hungerford, J.; Bhattacharyya, S.; Tumuluri, U.; Nair, S.; Wu, Z.; Walton, K. S. DMOF-1 as a Representative MOF for SO2 Adsorption in Both Humid and Dry Conditions. *J. Phys. Chem. C* **2018**, *122* (41), 23493–23500. https://doi.org/10.1021/acs.jpcc.8b06819.

(34) Kozachuk, O.; Meilikhov, M.; Yusenko, K.; Schneemann, A.; Jee, B.; Kuttatheyil, A. V; Bertmer, M.; Sternemann, C.; Pöppl, A.; Fischer, R. A. A Solid-Solution Approach to Mixed-Metal Metal–Organic Frameworks – Detailed Characterization of Local Structures, Defects and Breathing Behaviour of Al/V Frameworks. *Eur. J. Inorg. Chem.* **2013**, *2013* (26), 4546–4557. https://doi.org/https://doi.org/10.1002/ejic.201300591.

(35) Nouar, F.; Devic, T.; Chevreau, H.; Guillou, N.; Gibson, E.; Clet, G.; Daturi, M.; Vimont, A.; Grenèche, J. M.; Breeze, M. I.; Walton, R. I.; Llewellyn, P. L.; Serre, C. Tuning the Breathing Behaviour of MIL-53 by Cation Mixing. *Chem. Commun.* **2012**, *48* (82), 10237–10239. https://doi.org/10.1039/C2CC35348B.

(36) Klein, N.; Hoffmann, H. C.; Cadiau, A.; Getzschmann, J.; Lohe, M. R.; Paasch, S.; Heydenreich, T.; Adil, K.; Senkovska, I.; Brunner, E.; Kaskel, S. Structural Flexibility and Intrinsic Dynamics in the M2(2,6-Ndc)2(Dabco) (M = Ni, Cu, Co, Zn) Metal–Organic Frameworks. *J. Mater. Chem.* **2012**, *22* (20), 10303–10312. https://doi.org/10.1039/C2JM15601F.

(37) Dybtsev, D. N.; Chun, H.; Kim, K. Rigid and Flexible: A Highly Porous Metal-Organic Framework with Unusual Guest-Dependent Dynamic Behavior. *Angew. Chemie - Int. Ed.* **2004**, *43* (38), 5033–5036. https://doi.org/10.1002/anie.200460712.

(38) Wang, H.; Getzschmann, J.; Senkovska, I.; Kaskel, S. Structural Transformation and High Pressure Methane Adsorption of Co2(1,4-Bdc)2dabco. *Microporous Mesoporous Mater.*

2008, *116* (1), 653–657. https://doi.org/https://doi.org/10.1016/j.micromeso.2008.05.037.

(39) Maniam, P.; Stock, N. Investigation of Porous Ni-Based Metal–Organic Frameworks Containing Paddle-Wheel Type Inorganic Building Units via High-Throughput Methods. *Inorg. Chem.* **2011**, *50* (11), 5085–5097. https://doi.org/10.1021/ic200381f.

(40) Krause, S.; Hosono, N.; Kitagawa, S. Chemistry of Soft Porous Crystals: Structural Dynamics and Gas Adsorption Properties. *Angew. Chemie Int. Ed.* **2020**, *59* (36), 15325–15341. https://doi.org/https://doi.org/10.1002/anie.202004535.

(41) Bureekaew, S.; Amirjalayer, S.; Schmid, R. Orbital Directing Effects in Copper and Zinc Based Paddle-Wheel Metal Organic Frameworks: The Origin of Flexibility. *J. Mater. Chem.* **2012**, *22* (20), 10249–10254. https://doi.org/10.1039/C2JM15778K.

(42) Schneemann, A.; Vervoorts, P.; Hante, I.; Tu, M.; Wannapaiboon, S.; Sternemann, C.; Paulus, M.; Wieland, D. C. F.; Henke, S.; Fischer, R. A. Different Breathing Mechanisms in Flexible Pillared-Layered Metal-Organic Frameworks: Impact of the Metal Center. *Chem. Mater.* **2018**, *30* (5), 1667–1676. https://doi.org/10.1021/acs.chemmater.7b05052.

(43) Henke, S.; Schneemann, A.; Fischer, R. A. Massive Anisotropic Thermal Expansion and Thermo-Responsive Breathing in Metal–Organic Frameworks Modulated by Linker Functionalization. *Adv. Funct. Mater.* **2013**, *23* (48), 5990–5996. https://doi.org/10.1002/adfm.201301256.

(44) Henke, S.; Schneemann, A.; Wütscher, A.; Fischer, R. A. Directing the Breathing Behavior of Pillared-Layered Metal-Organic Frameworks via a Systematic Library of Functionalized Linkers Bearing Flexible Substituents. *J. Am. Chem. Soc.* **2012**, *134* (22), 9464–9474.

https://doi.org/10.1021/ja302991b.

(45) Henke, S.; Schneemann, A.; Fischer, R. A. Massive Anisotropic Thermal Expansion and Thermo-Responsive Breathing in Metal-Organic Frameworks Modulated by Linker Functionalization. *Adv. Funct. Mater.* **2013**, *23* (48), 5990–5996. https://doi.org/10.1002/adfm.201301256.

(46) Schwedler, I.; Henke, S.; Wharmby, M. T.; Bajpe, S. R.; Cheetham, A. K.; Fischer, R. A. Mixed-Linker Solid Solutions of Functionalized Pillared-Layer MOFs – Adjusting Structural Flexibility{,} Gas Sorption{,} and Thermal Responsiveness. *Dalt. Trans.* **2016**, *45* (10), 4230–4241. https://doi.org/10.1039/C5DT03825A.

(47) Rödl, M.; Kerschbaumer, S.; Kopacka, H.; Blaser, L.; Purtscher, F. R. S.; Huppertz, H.; Hofer, T. S.; Schwartz, H. A. Structural{,} Dynamical{,} and Photochemical Properties of Ortho-Tetrafluoroazobenzene inside a Flexible MOF under Visible Light Irradiation. *RSC Adv.* **2021**, *11* (7), 3917–3930. https://doi.org/10.1039/D0RA10500G.

(48) Jasuja, H.; Jiao, Y.; Burtch, N. C.; Huang, Y.; Walton, K. S. Synthesis of Cobalt-, Nickel-, Copper-, and Zinc-Based, Water-Stable, Pillared Metal–Organic Frameworks. *Langmuir* **2014**, *30* (47), 14300–14307. https://doi.org/10.1021/la503269f.

(49) Zhitomirsky, D.; Grossman, J. C. Conformal Electroplating of Azobenzene-Based Solar Thermal Fuels onto Large-Area and Fiber Geometries. *ACS Appl. Mater. Interfaces* **2016**, *8* (39), 26319–26325. https://doi.org/10.1021/acsami.6b08034.

(50) Olmsted, J.; Lawrence, J.; Yee, G. G. Photochemical Storage Potential of Azobenzenes. *Sol. Energy* **1983**, *30* (3), 271–274. https://doi.org/https://doi.org/10.1016/0038-

092X(83)90156-1.